Quantitative retardance imaging of biological samples using quadriwave lateral shearing interferometry

Sherazade Aknoun, Pierre Bon, Julien Savatier, Benoit Wattellier, Serge Monneret

HAL Id: hal-01203256

https://amu.hal.science/hal-01203256

Submitted on 22 Sep 2015

Quantitative retardance imaging of biological samples using quadriwave lateral shearing interferometry

Sherazade Aknoun,[1,2,*] **Pierre Bon,**[1,3] **Julien Savatier,**[1]
Benoit Wattellier,[2] **and Serge Monneret**[1]

[1]*Aix-Marseille Université, CNRS UMR 7249, Institut Fresnel, Campus de Saint-Jérôme, 13013 Marseille, France*
[2]*PHASICS SA, XTEC Bat. 404, Campus de l'Ecole Polytechnique, Route de Saclay, 91128 Palaiseau, France*
[3] *currently at CNRS, Institut d'Optique (LP2N), UMR 5298, Bordeaux Univ. Talence, France*
*sherazade.aknoun@fresnel.fr

Abstract: We describe a new technique based on the use of a high-resolution quadri-wave lateral shearing interferometer to perform quantitative linear retardance and birefringence measurements on biological samples. The system combines quantitative phase images with varying polarization excitation to create retardance images. This technique is compatible with living samples and gives information about the local retardance and structure of their anisotropic components. We applied our approach to collagen fibers leading to a birefringence value of $(3.4 \pm 0.3) \cdot 10^{-3}$ and to living cells, showing that cytoskeleton can be imaged label-free.

OCIS codes: (110.0180) Microscopy; (170.3880) Medical and biological imaging; (120.5050) Phase measurement; (290.3030) Index measurements.

References and links

1. E. Cuche, F. Bevilacqua, and C. Depeursinge, "Digital holography for quantitative phase-contrast imaging," Opt. Lett. **24**, 291–293 (1999).
2. B. Kemper and G. von Bally, "Digital holographic microscopy for live cell applications and technical inspection," Appl. Opt. **47**, A52–A61 (2008).
3. G. Popescu, T. Ikeda, R. R. Dasari, and M. S. Feld, "Diffraction phase microscopy for quantifying cell structure and dynamics," Opt. Lett. **31**, 775–777 (2006).
4. P. Bon, J. Savatier, M. Merlin, B. Wattellier, and S. Monneret, "Optical detection and measurement of living cell morphometric features with single-shot quantitative phase microscopy," J. Biomed. Opt. **17**(7), 076004 (2012).
5. M. Mir, Z. Wang, Z. Shen, M. Bednarz, R. Bashir, I. Golding, S. G. Prasanth, and G. Popescu, "Optical measurement of cycle-dependent cell growth," Proc. Natl. Acad. Sci. USA, **108**, 13124–13129 (2011).
6. P. Girshovitz and N. T. Shaked, "Generalized cell morphological parameters based on interferometric phase microscopy and their application to cell life cycle characterization," Biomed. Opt. Express **3**(8), 1757–1773 (2012).
7. T. A. Zangle and M. A. Teitell, "Live-cell mass profiling: an emerging approach in quantitative biophysics," Nat. Meth. **11**, 1221–1228 (2014).
8. M. Debailleul, V. Georges, B. Simon, R. Morin, and O. Haeberlé, "High-resolution three-dimensional tomographic diffractive microscopy of transparent inorganic and biological samples," Opt. Lett. **34**, 79–81 (2009).
9. W. Choi, C. Fang-Yen, K. Badizadegan, S. Oh, N. Lue, R. R. Dasari, and M. S. Feld, "Tomographic phase microscopy," Nat. Meth. **4**, 717–719 (2007).
10. Y. Cotte, F. Toy, P. Jourdain, N. Pavillon, D. Boss, P. Magistretti, P. Marquet, and C. Depeursinge, "Marker-free phase nanoscopy," Nat. Photon. **7**, 113–117 (2013).

11. B. Rappaz, P. Marquet, E. Cuche, Y. Emery, C. Depeursinge, and P. Magistretti, "Measurement of the integral refractive index and dynamic cell morphometry of living cells with digital holographic microscopy," Opt. Express **13**, 9361–9373 (2005).

12. P. Bon, S. Aknoun, S. Monneret, and B. Wattellier, "Enhanced 3D spatial resolution in quantitative phase microscopy using spatially incoherent illumination," Opt. Express **22**, 8654–8671 (2014).

13. R. Oldenbourg, E. Salmon, and P. Tran, "Birefringence of single and bundled microtubules," Biophys. J. **74**(1), 645–654 (1998).

14. F. Massoumian, R. Juskaitis, M. A. A. Neil, and T. Wilson, "Quantitative polarized light microscopy," J. Microsc. **209**(1), 13–22 (2003).

15. S. Sugita and T. Matsumoto, "Quantitative measurement of the distribution and alignment of collagen fibers in unfixed aortic tissues," J. Biomech. **46**, 1403–1407 (2013).

16. H. Nakaji, N. Kouyama, Y. Muragaki, Y. Kawakami, and H. Iseki, "Localization of nerve fiber bundles by polarization-sensitive optical coherence tomography," J. Neurosci. Meth. **174**, 82–90 (2008).

17. C. Fan and G. Yao, "Imaging myocardial fiber orientation using polarization sensitive optical coherence tomography," Biomed. Opt. Express **4**(3), 460–465 (2013).

18. A. Pierangelo, A. Benali, M.-R. Antonelli, T. Novikova, P. Validire, B. Gayet, and A. D. Martino, "Ex-vivo characterization of human colon cancer by mueller polarimetric imaging," Opt. Express **19**, 1582–1593 (2011).

19. M. W. Conklin, J. C. Eickhoff, K. M. Riching, C. A. Pehlke, K. W. Eliceiri, P. P. Provenzano, A. Friedl, and P. J. Keely, "Aligned collagen is a prognostic signature for survival in human breast carcinoma," Am. J. Pathol. **178**, 1221–1232 (2011).

20. C.E. Goldstein and H. Dennis, *Polarized Light*, Dennis Goldstein, ed. (CRC Press, 2003).

21. S.-Y. Lu and R. A. Chipman, "Interpretation of mueller matrices based on polar decomposition," J. Opt. Soc. Am. A **13**, 1106–1113 (1996).

22. C. L. Curl, C. J. Bellair, P. J. Harris, B. E. Allman, A. Roberts, K. A. Nugent, and L. M. Delbridge, "Quantitative phase microscopy: A new tool for investigating the structure and function of unstained live cells," Clin. Exp. Pharmacol. Physiol. **31**(12), 896–901 (2004).

23. Y. Kim, J. Jeong, J. Jang, M. W. Kim, and Y. Park, "Polarization holographic microscopy for extracting spatiotemporally resolved Jones matrix," Opt. Express **20**, 9948–9955 (2012).

24. Z. Wang, L. J. Millet, M. U. Gillette, and G. Popescu, "Jones phase microscopy of transparent and anisotropic samples," Opt. Lett. **33**, 1270–1272 (2008).

25. T. Tahara, Y. Awatsuji, Y. Shimozato, T. Kakue, K. Nishio, S. Ura, T. Kubota, and O. Matoba, "Single-shot polarization-imaging digital holography based on simultaneous phase-shifting interferometry," Opt. Lett. **36**, 3254–3256 (2011).

26. S.-Y. Lu and R. A. Chipman, "Homogeneous and inhomogeneous Jones matrices," J. Opt. Soc. Am. A **11**, 766–773 (1994).

27. N. M. Dragomir, X. M. Goh, C. L. Curl, L. M. D. Delbridge, and A. Roberts, "Quantitative polarized phase microscopy for birefringence imaging," Opt. Express **15**, 17690–17698 (2007).

28. N. Dragomir and A. Roberts, "Orientation independent retardation imaging using quantitative polarized phase microscopy," Microsc. Res. Tech. **75**(10), 1416–1419 (2012).

29. I. H. Shin, S.-M. Shin, and D. Y. Kim, "New, simple theory-based, accurate polarization microscope for birefringence imaging of biological cells," J. Biomed. Opt. **15**(1), 016028 (2010).

30. P. Bon, G. Maucort, B. Wattellier, and S. Monneret, "Quadriwave lateral shearing interferometry for quantitative phase microscopy of living cells," Opt. Express **17**, 13080–13094 (2009).

31. J. Primot and N. Guérineau, "Extended hartmann test based on the pseudoguiding property of a hartmann mask completed by a phase chessboard," Appl. Opt. **39**, 5715–5720 (2000).

32. P. Bon, S. Monneret, and B. Wattellier, "Noniterative boundary-artifact-free wavefront reconstruction from its derivatives," Appl. Opt. **51**, 5698–5704 (2012).

33. P. Bon, S. Lécart, E. Fort, and S. Lévêque-Fort, "Fast label-free cytoskeletal network imaging in living mammalian cells," Biophys. J. **106**(8), 1588–1595 (2014).

34. R. C. Jones, "A new calculus for the treatment of optical systems," J. Opt. Soc. Am. **31**, 488–493 (1941).

35. D. A. Lauffenburger and A. F. Horwitz, "Cell migration: A physically integrated molecular process," Cell **84**(3), 359–369 (1996).

36. H. Lodish and A. Berk, *Molecular Cell Biology*, 4th ed. (W. H. Freeman, 2000)

37. A. Bhattacharjee and M. Bansal, "Collagen structure: the madras triple helix and the current scenario," IUBMB Life **57**(3), 161–172 (2005).

38. F. P. Bolin, L. E. Preuss, R. C. Taylor, and R. J. Ference, "Refractive index of some mammalian tissues using a fiber optic cladding method," Appl. Opt. **28**, 2297–2303 (1989).

39. J. Riedl, A. H. Crevenna, K. Kessenbrock, J. H. Yu, D. Neukirchen, M. Bista, F. Bradke, D. Jenne, T. A. Holak, Z. Werb, M. Sixt, and R. Wedlich-Soldner, "Lifeact: a versatile marker to visualize f-actin," Nat. Meth. **5**, 605–607 (2008).

1. Introduction

Changes in the refractive index inside the sample is the major contrast source in optical phase microscopy of living cells. Moreover, quantitative phase techniques [1–4] are now establishing in microscopy for measuring specific properties of semi-transparent samples, like the dry mass of living cells applied to cell growth and division studies [5–7]. Recently, tomographic approaches using Quantitative Phase Imaging (QPI) have shown the possibility to make 3D reconstructions of biological samples using different setups [8–12]. The strength of those techniques is their non-invasive and fast approach. However, the contrast only comes from the local optical path difference of the object, so that it may be difficult in some cases to identify small substructures inside a given sample.

It is now well known that cytoskeleton inside cells, or collagen fibers inside tissues, are optically anisotropic and thus scatter light differently depending on the illumination light polarization. This has been exploited to reveal ordered fibrous structures in biological samples without any staining or labelling with polarized light microscopy [13–15] or polarization sensitive optical coherence tomography [16, 17]. Recent studies have shown polarimetry as a potential diagnostic tool for various dermatological diseases on thick tissue samples, as polarimetric properties of media are directly linked to their organization [18]. Particularly, specific collagen fibers spatial distribution has been recently demonstrated to be a signature for the optical diagnosis and prognosis of cancer in tissues [19].

Polarimetry is an experimental technique for deducing the polarizing properties of a birefringent medium by measuring the polarization state of a light beam after its propagation through it. Changes in the polarization state can be represented by a Jones matrix for fully polarized light, or by a Mueller matrix for partially polarized light. The Mueller formalism leads to a complete medium characterization and identification [20] even for a depolarizing medium. However, its experimental determination implies in general a minimal set of 16 measurements and needs matrix decompositions [21]. In the scope of living semi-transparent biological sample imaging, this approach may be too slow and requires a heavy formalism.

QPI techniques are quite adapted to process quantitative polarimetry using Jones formalism [22–25] as they give access to both intensity and phase information. One can retrieve the total electromagnetic field and deduce quantitative information about specimen polarimetric properties like birefringence or dichroism. Although less determination terms are needed compared to the Mueller formalism, polarization properties extraction from Jones matrices still requires a relatively complex numerical process [26].

Some faster methods, which allow fast linear birefringence extraction, have been proposed recently [27, 28]. However, they require *a priori* knowledge about the sample and few are fast enough to deal with living biological samples [29].

In a previous paper, we proposed the use of a wave front sensor based on quadri-wave lateral shearing interferometry (QWLSI) placed in the image plane of an inverted microscope, in order to realize quantitative phase imaging [30]. QWLSI is based on the interferences of four replicas of an incident wave-front. The replicas are created by a bidimensional and quasi-bisinusoidal diffraction grating called Modified Hartmann Mask (MHM) [31]. The superposition of those replicas creates, after a small propagation, an interferogram that is recorded by a CCD camera and next analyzed by a numerical Fourier transform. This allows to extract both the intensity and Optical Path Difference (OPD) along the two space directions of the electromagnetic field [30,32]. This highly contrasted QPI reveals cellular components giving quantitative information about them [33].

In this paper, we propose to extend this technique to the measurement of quantitative local retardance. Employed with polarized illumination, it is used to measure a set of polarization-dependent phase shifts, in order to reveal samples anisotropic structures inside biological living

samples (see Fig. 1).

Polarization dependency adds specificity to our method allowing contrast enhancement and retardance measurements of anisotropic structures in the sample.

Jones formalism is used to describe the electric field measured by QWLSI. The set of the different polarimetric images is numerically computed to obtain what we call "Quantitative Retardance Images" which give at once spatial distributions of local retardance and optical axis orientation in the sample.
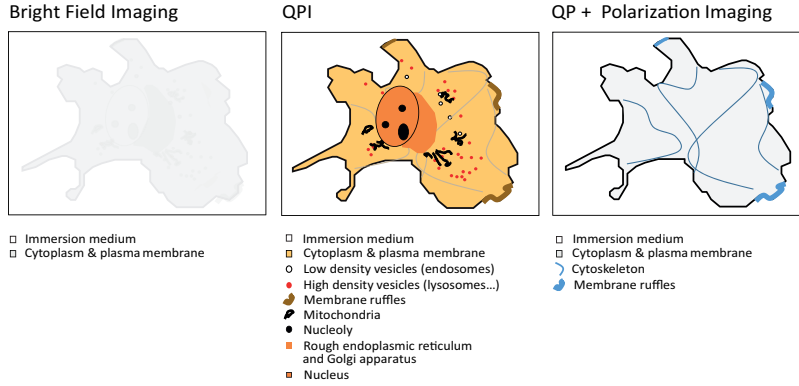

Fig. 1. Schematic view presenting the interest of introducing polarized light into QPI.

2. Theory

In this part, we will establish the QWLSI interferogram equation, obtained with polarized light, and the expression of the resulting OPD.

2.1. OPD measurement under polarized light

For sake of simplicity, we will consider a one-dimensional model here as the extension to two dimensions is straightforward. The equation of a 1-D QWLSI interferogram is given by [30]:

$$I_{meas} = I_0 \cdot [1 + \cos(\frac{2\pi}{p}(x - z\frac{\partial OPD}{\partial x}))]$$ (1)

where I_0 is the incident electromagnetic field intensity, p, the diffraction grating period, z, the distance between the grating and the sensor and $\frac{\partial OPD}{\partial x}$, the OPD gradient along $\vec{x}$.

The OPD gradient is extracted from the modulated intensity using the formula:

$$\frac{\partial OPD_{meas}}{\partial x} = \frac{p}{2\pi z} \cdot arg\left[\mathscr{F}\mathscr{T}^{-1}\left[\mathscr{F}\mathscr{T}(I_{meas}) \otimes \delta(k - \frac{1}{p})\right]\right].$$ (2)

where arg is the argument function, $\mathscr{F}\mathscr{T}$ the Fourier transform, $\mathscr{F}\mathscr{T}^{-1}$, the inverse Fourier transform. To obtain individual images for intensity and OPD gradients, a low-pass filtering is also applied by Fourier space clipping around k = 0 and k = 1/p.

Using a linearly polarized plane wave, we define the Optical Path Difference, OPD, as follows:

$$OPD = \int_0^t (n(\theta) - n_{medium}) \cdot dz$$ (3)

where θ is the polarization angle of the plane wave with respect to the laboratory axes system, $n(\theta)$ and n_{medium} are the local refractive indices of respectively the sample and the surrounding medium and t is the mechanical thickness of the sample along the optical axis.

Let us now consider an arbitrary polarized incident plane wave which electric field is given by: $\vec{E} = E_x \cdot \vec{x} + E_y \cdot \vec{y}$, E_x and E_y being complex numbers and $\vec{x}$, $\vec{y}$ two vectors defining the main axis system. We will now derive the interferogram intensity captured by the wave front sensor camera. As two orthogonally polarized beams cannot interfere one with the other, the interferogram will be then formed by the incoherent sum of the two elementary interferograms generated by the electromagnetic fields E_x and E_y. As a consequence, we will consider intensity $I_{0x,y}$ and $OPD_{x,y}$ associated to each incident light polarization along $\vec{x}$ and $\vec{y}$, which leads to the following interferogram intensities:

$$I_x = I_{0x} \cdot \left[1 + \cos\left(\frac{2\pi}{p}\left(x - z\frac{\partial OPD_x}{\partial x}\right)\right)\right] \tag{4}$$

$$I_y = I_{0y} \cdot \left[1 + \cos\left(\frac{2\pi}{p}\left(x - z\frac{\partial OPD_y}{\partial x}\right)\right)\right] \tag{5}$$

We express the total measured intensity $I_{tot} = I_x + I_y$ using Eqs. (1) and the intensities along x and y (Eqs. (4) and (5)):

$$I_{tot} = I_{0x} + I_{0y} + \frac{1}{2} \cdot \left[\exp\left(\frac{2i\pi x}{p}\right) \cdot \left(I_{0x} \cdot \exp\left(\frac{-2i\pi z}{p}\cdot\frac{\partial OPD_x}{\partial x}\right) + I_{0y} \cdot \exp\left(\frac{-2i\pi z}{p}\cdot\frac{\partial OPD_y}{\partial x}\right)\right) \right. \tag{6}$$
$$\left. + \exp\left(\frac{-2i\pi x}{p}\right) \cdot \left(I_{0x} \cdot \exp\left(\frac{2i\pi z}{p}\cdot\frac{\partial OPD_x}{\partial x}\right) + I_{0y} \cdot \exp\left(\frac{2i\pi z}{p}\cdot\frac{\partial OPD_y}{\partial x}\right)\right)\right].$$

We analyze the interferogram to retrieve the total intensity and the OPD gradient by taking the Fourier transform (FT) of the previous expression and write:

$$\mathscr{F}\mathscr{T}(I_{tot}) = \mathscr{F}\mathscr{T}(I_{0x} + I_{0y}) + \frac{1}{2}\cdot\delta\left(k - \frac{1}{p}\right)\otimes\mathscr{F}\mathscr{T}\left[I_{0x}\cdot\exp\left(\frac{-2i\pi z}{p}\cdot\frac{\partial OPD_x}{\partial x}\right) \right. \tag{7}$$
$$\left. + I_{0y}\cdot\exp\left(\frac{-2i\pi z}{p}\cdot\frac{\partial OPD_y}{\partial x}\right)\right] + C.C$$

where C.C is the complex conjugate.

Using Eq. (2), we demodulate around the $\frac{1}{p}$ spatial frequency to extract the OPD gradient along $\vec{x}$ using:

$$\nabla OPD_{meas} = \frac{1}{\alpha}\cdot arg(I_x \cdot e^{i\alpha\nabla OPD_x} + I_y \cdot e^{i\alpha\nabla OPD_y}) \tag{8}$$

The parameter $\alpha = \frac{2\pi z}{p}$ is linked to the QWLSI interferometer characteristics (*i.e.* grating pitch and distance between the sensor and the grating), ∇OPD_x and ∇OPD_y are the OPD gradients for each polarization and *arg* is the argument function.

The aim of the following is to express ∇OPD_{meas} as a function of ∇OPD_x and ∇OPD_y. First, we can rewrite the expression in the argument function as:

$$e^{i\frac{\alpha(\nabla OPD_x + \nabla OPD_y)}{2}}\left(I_x e^{i\frac{\alpha(\nabla OPD_x - \nabla OPD_y)}{2}} + I_y e^{-i\alpha\frac{(\nabla OPD_x - \nabla OPD_y)}{2}}\right). \tag{9}$$

Using the following expression $Ae^{i(x-y)} + Be^{-i(x-y)} = (A+B)\cos(x-y) + i(A-B)\sin(x-y)$, we can write the previous established expression differently:

$$e^{i\frac{\alpha(\nabla OPD_x + \nabla OPD_y)}{2}} \left[(I_x + I_y)\cos\left(\frac{\alpha(\nabla OPD_x - \nabla OPD_y)}{2}\right) + \atop i(I_x - I_y)\sin\left(\frac{\alpha(\nabla OPD_x - \nabla OPD_y)}{2}\right) \right] \tag{10}$$

Taking the argument of the previous expression, we obtain:

$$\nabla OPD_{meas} = \frac{(\nabla OPD_x + \nabla OPD_y)}{2} + \frac{1}{\alpha}\arctan\left(\frac{I_x - I_y}{I_x + I_y}\cdot\tan\left((\alpha\nabla OPD_x - \alpha\nabla OPD_y)/2\right)\right) \tag{11}$$

If we consider that the measured retardance is weak, we can simplify the previous expression (the calculation is shown in Appendix A) and obtain the following expression:

$$\nabla OPD_{meas} \approx \frac{I_x\nabla OPD_x + I_y\nabla OPD_y}{I_x + I_y}. \tag{12}$$

We can see that the measured OPD gradient is an average value of the gradients along the two directions x et y, where each gradient is weighted by the correspondent intensity.

A numerical application is realized in Appendix A. We can deduce that the maximum value difference between the two OPD gradients needs to be lower than 346 nm over two OPD pixels in the microscope image plane (where the wave front sensor is located), which is mostly the case for biological samples. If this variation is too high, it is noteworthy that we can adjust the magnification to spread the information on more pixels to obtain a weaker local gradient. In case the intensity along one direction is weak, its contribution to the measured OPD will be weak.

2.2. Birefringence measurement

The purpose of this second part is to link the electromagnetic field measured by the sensor which expression has been previously established to the sample optical properties.

2.2.1. Electromagnetic field transmitted by a birefringent medium

One cause of modification in the light's polarization state is a change in the relative phase shift between the vectorial components of the electric field $\vec{E}$. If light propagates through an anisotropic medium, these components will see different refractive indices depending on their orientation. For an uniaxial birefringent medium, those refractive indices only depend on the angle between the polarization direction and the optical axis of the medium.

We work with an electrical field: $\vec{E} = [E_x, E_y, 0]$ which propagates through our sample along $\vec{z}$. The sample is assumed to be linearly birefringent with its optical axis contained in the XY plane and oriented with an angle θ_o relative to the laboratory horizontal axis $\vec{x}$. In that way, the birefringence is considered to be constant along the optical axis $\vec{z}$ (Fig. 2(a)).

Using Jones formalism [34], the output electric field E_{out} can be expressed by :

$$\vec{E}_{out} = (J)\cdot\vec{E}_{in} \tag{13}$$

where $\vec{E}_{in}$ is the incident electric field, (J) a matrix related to the sample Jones matrix (J_{sample}) in the crystal principal axis frame by

$$(J) = (R-(\theta-\theta_0))\cdot(J_{sample})\cdot(R(\theta-\theta_0))$$

and R is the rotation matrix defined by

$$R(\theta - \theta_0) = \begin{pmatrix} \cos(\theta - \theta_0) & -\sin(\theta - \theta_0) \\ \sin(\theta - \theta_0) & \cos(\theta - \theta_0) \end{pmatrix} \qquad (14)$$

as the sample optical axes system is linked to the laboratory's one by a simple rotation of θ_0 angle. In the $(\vec{u}_o, \vec{u}_e)$ axis system, the Jones matrix J_{sample} for a homogeneous and uniaxial birefringent specimen of thickness t, which is essentially a linear retarder, can be written as:

$$(J_{sample}) = \begin{pmatrix} e^{ik\delta o} & 0 \\ 0 & e^{ik\delta e} \end{pmatrix} \qquad (15)$$

with $e^{ik\delta o}$ and $e^{ik\delta e}$ such as $k = \dfrac{2\pi}{\lambda}$, $\delta o = (n_o - n_{medium}) \times t$ and $\delta e = (n_e - n_{medium}) \times t$ where λ is the average wavelength, t the mechanical thickness of the sample, n_e and n_o respectively the extraordinary and ordinary refractive indices which define the birefringence as $\Delta n = (n_e - n_o)$ of an uniaxial sample.

The retardance can be written $\Delta\delta = \delta e - \delta o = \Delta n \times t$.

Using $\alpha = e^{ik\delta o}$ and $\beta = e^{ik\delta e}$, we can write in the $(\vec{u}_x; \vec{u}_y)$ system, where $\vec{u}_x$ and $\vec{u}_y$ are unit vectors along respectively $\vec{x}$ and $\vec{y}$:

$$(J) = \left(\frac{\alpha + \beta}{2}\right) \begin{pmatrix} 1 & 0 \\ 0 & 1 \end{pmatrix} + \left(\frac{\alpha - \beta}{2}\right) \begin{pmatrix} \cos 2(\theta - \theta_0) & \sin 2(\theta - \theta_0) \\ \sin 2(\theta - \theta_0) & -\cos 2(\theta - \theta_0) \end{pmatrix} \qquad (16)$$

Let us now consider $\vec{E}_{in} = ||\vec{E}_{in}|| \cdot [1, 0]$ in the $(\vec{u}_x; \vec{u}_y)$ system. Equation (13) gives:

$$\vec{E}_{out} = \left[\left(\frac{\alpha + \beta}{2}\right) \begin{pmatrix} 1 \\ 0 \end{pmatrix} + \left(\frac{\alpha - \beta}{2}\right) \begin{pmatrix} \cos 2(\theta - \theta_0) \\ \sin 2(\theta - \theta_0) \end{pmatrix} \right] \cdot ||\vec{E}_{in}|| \qquad (17)$$

Using the relations : $\left(\dfrac{\alpha + \beta}{2}\right) = \cos\left(\dfrac{k \cdot \Delta\delta}{2}\right) \cdot e^{\frac{ik(\delta o + \delta e)}{2}}$ and $\left(\dfrac{\alpha - \beta}{2}\right) = i \cdot \sin\left(\dfrac{k \cdot \Delta\delta}{2}\right) \cdot e^{\frac{ik(\delta o + \delta e)}{2}}$, we can write:

$$\vec{E}_{out} = ||\vec{E}_{in}|| \cdot e^{\frac{ik(\delta o + \delta e)}{2}} \cdot \left[\left(\cos\left(\frac{k \cdot \Delta\delta}{2}\right) + i \cdot \sin\left(\frac{k \cdot \Delta\delta}{2}\right) \cdot \cos 2\left(\theta - \theta_0\right) \right) \cdot \vec{u}^{\parallel} \right.$$
$$\left. + \left(i \cdot \sin\left(\frac{k \cdot \Delta\delta}{2}\right) \cdot \sin 2\left(\theta - \theta_0\right) \right) \cdot \vec{u}^{\perp} \right] \qquad (18)$$

When $(\theta - \theta_0) = 0°$ or $(\theta - \theta_0) = 90°$, Eq. (18) shows that the output field has the same polarization direction as the input one but exhibits a phase shift corresponding respectively to the ordinary or the extraordinary OPD. For other angles, it is not possible to give a simple analytical formula for the OPD and the measured wave front interpretation is not trivial. Nevertheless, we will show that for low retardance values, the measured OPD varies sinusoidally with the incident polarization angle.

2.2.2. Measurement on weakly retardant samples

We establish an expression for the intensity along $\vec{u}^{\parallel}$ from Eq. (18):

$$I_{out}^{\parallel} = I_0 \left[\cos^2\left(\frac{k\Delta\delta}{2}\right) + \sin^2\left(\frac{k\Delta\delta}{2}\right) \cos^2\left(2(\theta - \theta_0)\right) \right]. \qquad (19)$$
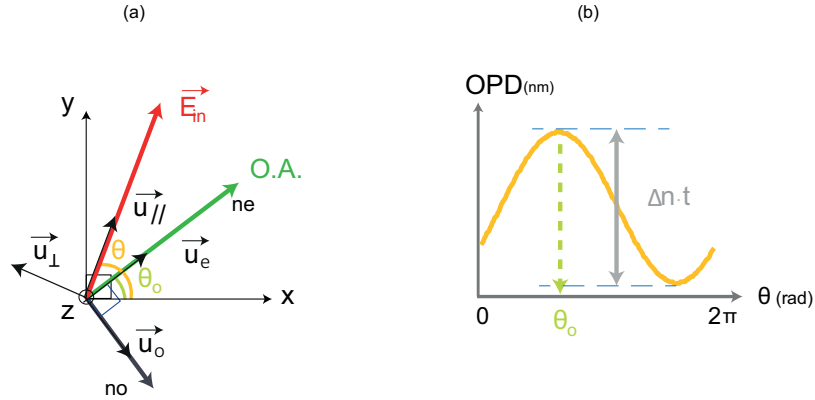
Fig. 2. Illustration of the polarization dependent OPD measurement principle. (a) Schematic representations of the different axes systems and (b) the OPD variation with the light polarization orientation with respect to an initial value for an anisotropic object. $\vec{E}_{in}$ is the incident electric field vector, O.A. refers to the sample optical axis, (x,y,z) is the main axis system, e and o indices refer to respectively *extraordinary* and *ordinary*, $\parallel$ and $\perp$ indices refer respectively to parallel and perpendicular axis respectively to the incident electric field. Δn is the local retardance, t the mechanical thickness and θ_0 is the orientation of the sample optical axis in the main axis system.

Using $\cos^2(\alpha) = 1 - \sin^2(\alpha)$ and $\sin^2(\theta) = 1/2 \cdot (1 - \cos(2\theta))$, we can write:

$$I_{out}^{\parallel} = I_0 \left[1 - \frac{1}{2} \sin^2 \left(\frac{k\Delta\delta}{2} \right) (1 - \cos(4(\theta - \theta_0))) \right]. \tag{20}$$

From this expression, we can imagine an experiment where the intensity would be measured after an analyzer which polarization direction is synchronized with the input polarizer. The intensity data would be fitted by a sinusoidal function which parameters would lead to the birefringence parameters (refractive indices, optical axis direction). Since the intensity is always sinusoidal, this allows high retardance measurements. However, for weak retardance samples, since the obtained parameter $\sin^2 \left(\frac{k\Delta\delta}{2} \right)$ varies quadratically with the retardance $\Delta\delta$, the request signal-to-noise ratio (SNR) makes this method quite insensitive. In this paper, we will show that phase is more adapted in this case as the recovered parameters varies linearly with the retardance.

We now evaluate the normalised values of $I_{out}^{\parallel}$ and $I_{out}^{\perp}$. We represent those intensities from Eq. (18) in function of θ for different retardance values to see the repartition of the total intensity along the two directions. Results are shown in Fig. 3.

We can see that up to 3 µm of retardance, intensity is mostly along $\vec{E}_{out}^{\parallel}$ with more than 99% of the total intensity. For a $\Delta\delta$ of 10 µm, we can see that we have, for some values of θ, $I_{out}^{\perp}$ of 20% of the total intensity. Thanks to this result, we can consider that $\vec{E}_{out}$ for weakly retardant samples is essentially oriented along $\vec{u}^{\parallel}$. For samples of retardance lower than 1 µm, in the case where there is no cross-talk from one polarization to an other, the second term of Eq. (18) along $\vec{u}^{\perp}$ can be neglected for the OPD measurement since the intensity component along the orthogonal direction to the incident polarization is weak.

Experimentally, following the incident polarization is complicated and can be an additional source of noise. To avoid this, this hypothesis, verified later thanks to simulations in section 2.3, allows us to make measurements without polarized detection.
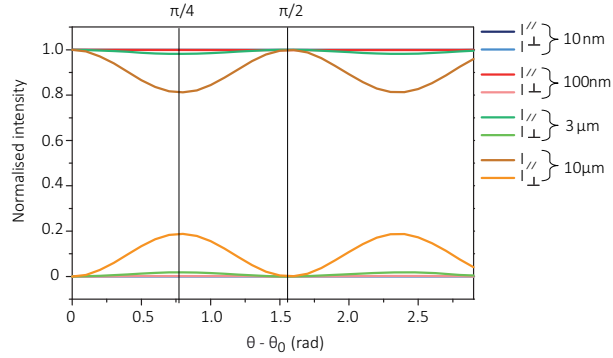
Fig. 3. Representation of normalised intensity along parallel and perpendicular directions in function of θ.

In the following, we will demonstrate the influence of the orthogonal part of the electric field on phase measurement. We will define the experimental parameters for which we will neglect the effect of this component upon phase measurements. We will now derive the expression of the measured OPD under the following assumption : only the parallel component of the electric field contributes to the measured OPD.

2.2.3. Parallel polarization OPD

Let us consider the expression of $\vec{E}_{out}^{\parallel}$:

$$\vec{E_{out}} = ||\vec{E_{in}}||e^{\frac{ik(\delta o + \delta e)}{2}}\left(\cos\left(\frac{k\Delta\delta}{2}\right) + i\sin\left(\frac{k\Delta\delta}{2}\right)\cos 2(\theta - \theta_0)\right)\vec{u}^{\parallel}. \tag{21}$$

We want to determine the variation of OPD_x, the argument of this complex field $\vec{E_{out}}$. In the case of $\Delta\delta$ weak, we expect a periodic but also sinusoidal variation of the polarization angle.

After calculation (see Appendix B), we consider OPD_x as purely sinusoidal of period π if $(\frac{\Delta\delta^3}{96}\frac{\pi^2}{\lambda^2})$ is negligible in front of $\frac{\Delta\delta}{2}$. This is true if $\Delta\delta \ll \frac{4\sqrt{3}\lambda}{\pi}$, with $\frac{4\sqrt{3}}{\pi} \approx 2,2$.

In conclusion, for retardance values such as $\Delta\delta << 2,2\lambda$, OPD varies as a sinusoidal function of the incident polarization angle and:

$$OPD_{measured}(\theta) = \frac{(\delta o + \delta e)}{2} + (\frac{\Delta\delta}{2})\cos 2(\theta - \theta_0). \tag{22}$$

2.2.4. Birefringence parameters from OPD measurement series

From Eq. (22), we will measure $\Delta\delta$ and θ_0 making θ vary. In order to extract parameters of interest, we successively record a set of N interferograms corresponding to N values of θ_0 (polarized orientation) equally distributed in the $[0, \pi]$ range. We thus obtain a N-values sampling of $OPD(\theta)$ as defined by Eq. (22). We fit this function by a sine curve of equation:

$$OPD(\theta) = A + B \cdot \cos(2\theta) + C \cdot \sin(2\theta) \tag{23}$$

where A = $\frac{\delta_o + \delta_e}{2}$, B = $\frac{\Delta\delta}{2} \cdot \cos(2\theta_0)$ and C = $-\frac{\Delta\delta}{2} \cdot \sin(2\theta_0)$.

From this fit, three parameters are extracted: $\Delta\delta$, $\frac{(\delta o + \delta e)}{2}$ and θ_0.

To sum up, experiments are done as illustrated in Fig. 4: a set of N OPD images is taken, for N values of θ_0 corresponding to varying incident linear polarization directions. These images are then numerically processed pixel by pixel. For each pixel, a curve is obtained and fitted using Eq. (23), allowing extraction of local retardance parameters. Then, complete images representing $\Delta\delta$ or θ_0 distributions can be proposed, where anisotropic elements are highlighted.
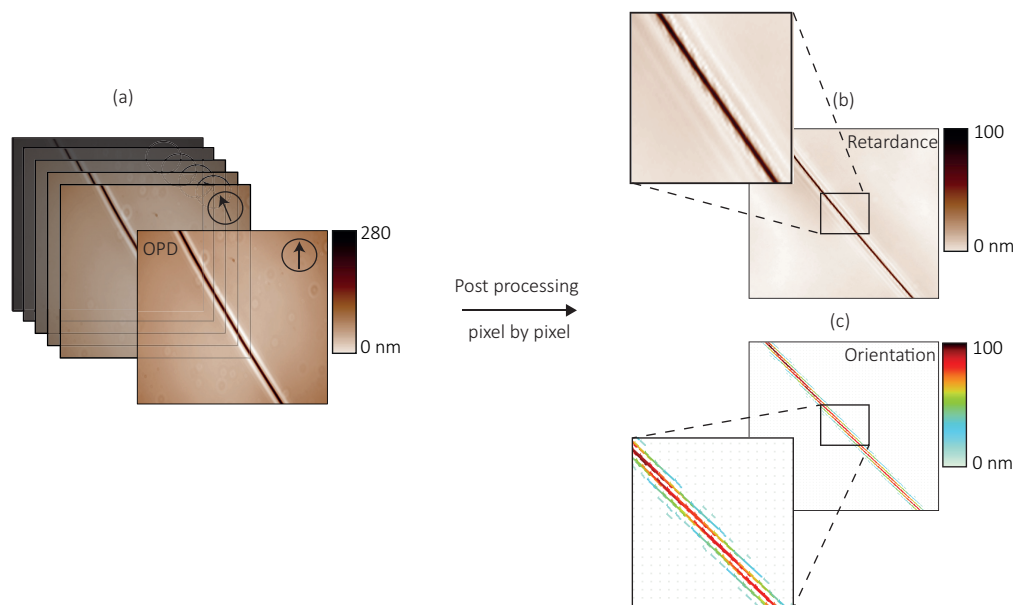

Fig. 4. Illustration of the post processing principle of the (a) OPD polarized stack of images in order to create numerically two images of (b) retardance and (c) orientation dependant contrast.

2.3. Method validation by simulations

To evaluate the validity domain of our technique and subsequent error made on the retardance measurement, a simulation tool has been implemented. In this section, we study the effect of large retardance values on the OPD measured by the wave front sensor, when the output light is directly sent to it. We show that because the QWLSI measures the wave front gradients, the measurement dynamic range is very large even when the intensity in the perpendicular component becomes significant. This is explained by the fact that this component is a pure imaginary number so that its phase is always $\frac{\pi}{2}$ and thus its gradient vanishes for any polarization and pixel.

We used a numerical birefringent phase object of thickness $t = t_0 \cdot e^{-x^2/a^2}$, where a is a parameter to control the object width which is chosen to obtain a correct sampling of the object on the OPD image. We chose its birefringence value such as $\Delta n = 10^{-2}$ and $n_{medium} = 1.33$ to match with typical biological samples placed in water-based solutions. The retardance amplitude is tuned by changing the sample thickness.

From this object, we generated complete interferograms as the sum of the two elementary interferograms generated by $\vec{E}_{out,x}$ and $\vec{E}_{out,y}$, each of them being calculated as described in [30]. This operation was reported for different θ_0 values in order to build a set of N complete interferograms that were post-processed to recover the N associated OPD images.
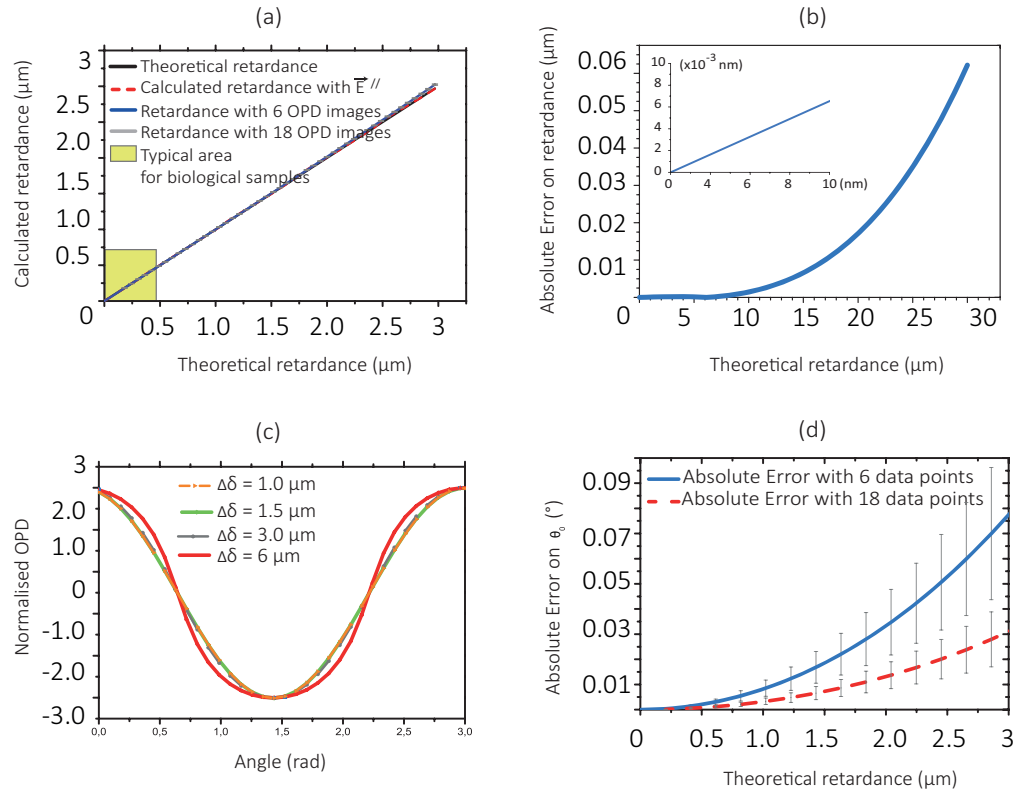
Fig. 5. (a) Results of retardance measurements calculated for retardance values from 0 to 3 μm by using 6 polarization angles to constitute the requested set of OPD images that are post-processed to determine the retardance. (b) Absolute measurement error calculated for retardance values from 0 to 3 μm with N=6. (c) Normalised OPD for different retardance values and (d) Absolute error on θ_0 versus the theoretical retardance with N=6 or N=18 polarization angles.

Then, OPD images were processed pixel by pixel and fitted as it has been described for experimental data analysis.

We choose to do these simulations for theoretical retardance values $\Delta\delta$ from 0 to 3 μm obtained by varying the thickness of the simulated object. For biological samples that are of interest in our applications, typical retardance values are from 10 to 200 nm.

Results are shown in Fig. 5. This figure shows the theoretical retardance and the retrieved one when 6 polarization angles are considered to fit $\Delta\delta$. The corresponding absolute error for the retardance measurement in function of the theoretical retardance is plotted Fig. 5(b). We can see that for retardance values below 1 μm, this error is less than $1.7\cdot10^{-3}$ μm as soon as the set of images is composed at least of 6 different angles.

The error made is essentially due to the shape of the sinusoidal curve which becomes less sinusoidal as the retardance value increases and the influence of the perpendicular component increases. The phenomenon is illustrated in Fig. 5(c). Indeed for this upper part of the dynamic range, a better estimator for $\Delta\delta$ is given by $|OPD_{max} - OPD_{min}|$. For θ_0 determination, we see that the absolute error is less than 4 degrees when using 6 polarization angles and less than 2 degrees using 18 polarization angles for high retardance values (Fig. 5(d)). Using 18 polarisation
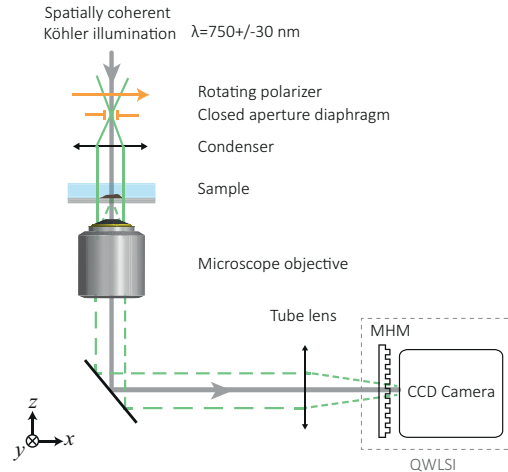
Fig. 6. Experimental setup scheme.

angles does not lead to a more precise retardance measurement. However, for fixed samples, where there is no problem of acquisition time, 18 OPD images will be taken to reconstruct retardance information to sample correctly the experimental curve and reduce the error on the orientation measurement.

Thanks to this simulation, we can validate our method and neglect what we call cross-talk *i.e.* the transfer from the polarization axis to the orthogonal one for objects of retardance values up to 1 μm.

Experimentally, this assumption leads to a strongly simplified setup by working without any polarization analyzer before the QWLSI system.

3. Experimental validation

3.1. Setup for QWLSI

The experimental setup, shown in Fig. 6, is composed of a non-modified inverted microscope (TE2000-U, Nikon, Japan) on which we added a 750 ± 30 nm bandpass filter in order to avoid sample refractive index dispersion and to work with near IR which is weakly absorbed by living cells. We used Nikon objectives (magnification $40\times$, $NA = 1.3$ and $NA = 0.75$ and magnification $100\times$, $NA = 1.3$) and a 400 mm tube lens to realize an additional $2 \times$ magnification in order to have a good sampling with our QWLSI. We worked with a transmission Köhler illumination and closed the aperture diaphragm to have a high spatial light coherence. This allows to assume that a plane wave propagating along the optical axis illuminates the sample orthogonally to its (x,y) plane. The QWLSI (SID4Bio, Phasics SA, Palaiseau, France) was mounted on a C-mount adapter on one modified microscope's camera port so that the detector plane matches the microscope image plane with the additional 400 mm focal tube lens. A linear polarizer (LPVIS100, Thorlabs, USA) is placed in a rotating support (NewStep NSR Series Universal Rotator, Newport, US) and into the illumination light path before the sample and above the microscope closed aperture diaphragm in order to drive the polarization direction of incident field.
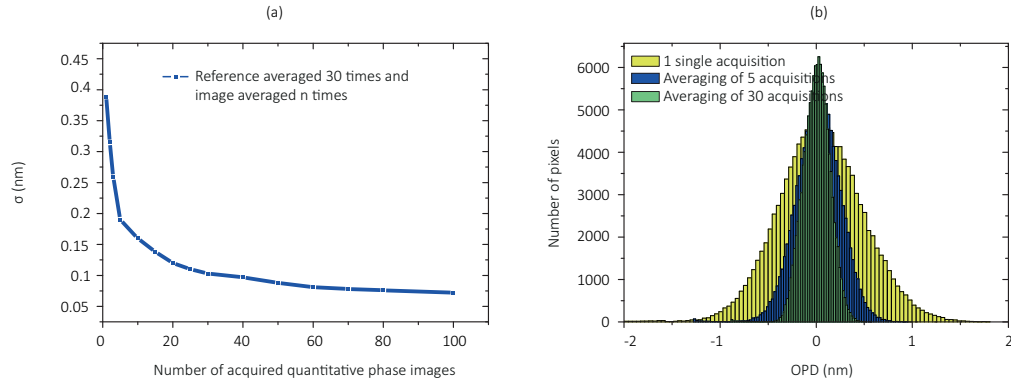
Fig. 7. (a) OPD spatial standard deviation from a sample empty area, versus the number of averaged successive acquisitions. 80 *times* magnification, NA=1.3. Exposure time = 15 ms. (b) OPD histogram evolution with the number of averaged acquisitions.

3.2. *Optical axis direction calibration protocol*

We choose to process two types of images: a linear retardance dependant image which reveals the anisotropic components of the sample and a second image that gives structural orientations with respect to the laboratory axis system. We choose to represent the local optical axes orientation by a line which orientation gives θ_0. The line length is proportional to the retardance value also represented with a color map for better visualization.

To reference the 0° polarization angle direction, the rotating polarizer was placed between two crossed polarizers prior to the measurements with respective optical axis along x and y axes (defined as the laboratory axes) so as to define the optical axis of the rotating polarizer. This was considered to plot the orientation of the local optical axis of the samples during the experiments.

3.3. *Retardance measurement errors*

Before illustrating with different biological examples, we evaluated the different sources of uncertainty and error for our retardance measurements.

3.3.1. Acquistion noise

The first one comes directly from the noise of the OPD imaging step (*i.e.* the fundamental acquisition process that is required to record each reference and OPD images for each polarization direction). This is mostly limited by the camera noise (read and shot noise) and reduced by averaging multiple acquisitions.

We first calculated the evolution of the OPD standard deviation distribution of a sample empty area of 300x400 pixels when a time-averaging of N successive interferograms occurred. More precisely, we averaged both reference interferograms (N = 30) and acquisition ones (varying N) with an 80 × magnification, NA= 0.75 and an exposure time of 15 ms. Results are summed up in Fig. 7(a). From these results, we decided for experiments to fix N= 30 for reference step and N = 5 for the actual imaging process. In these conditions, standard deviation value of the OPD is 0.25 nm.
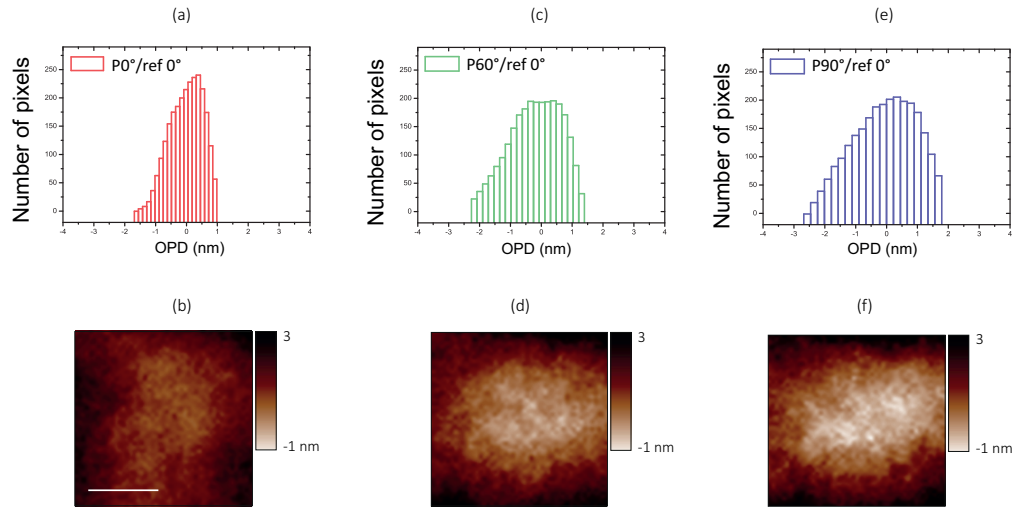
Fig. 8. (a, c & e) Distribution of OPD values of empty sample areas. The three OPD images recovered from interferogrames acquired in an sample-free region respectively at (b) 0, (d) 60 and (f) 90° polarization angles are associated with a unique reference interferogram taken at 0° polarization angle. The standard deviation value of the pixels is calculated and we can see that its maximal value is reached for the association of reference taken at 0° and image taken at 90° polarisation angles. Scale bar represents 6 μm. (NA=1.3 x80 magnification observation, exposure time = 25 ms.)

3.3.2. Reference

In order to take into account static effects introduced by the optical components themselves (objective, illumination optics), we are used to record, before beginning the measurements, a stack of polarized reference wave fronts in an element-free region of the sample [4]. Then, the static OPD distribution is processed from this reference wavefront, and it will be systematically subtracted to all subsequent acquisitions.

We studied the effect of using the same reference image for different polarization angles without any sample in the field of view. In this work, additional polarization-dependant static aberrations have to be taken into account, as shown on Fig. 8. In this figure, we give OPD images of empty sample areas for different polarization directions, but using a single reference interferogram. One can clearly note a significant enlargement of OPD distribution values when the difference between polarization directions of reference and measurement increases.

The standard deviation value of OPD images shown in Figs. 8(a), 8(b) and 8(c) was calculated. With the right interferogram association, we obtain a standard deviation value of 0.62 nm. With the two others associations, we obtain higher values as we can also see with the representation in histogram: 0.85 (for an image interferogram taken at 60° and reference interferogram taken at 0°) and 1.05 nm (for interferogram taken at 90° and reference interferogram taken at 0°). We conclude that OPD acquired in the microscope optical pathway varies with the polarization. Low spatial frequencies probably due to birefringence in the objectives are visible on the Fig. 8 OPD maps.

As a consequence, we have to record a set of reference wavefronts according to θ chosen values, and next use adequate reference data for post-processing. In conclusion, the measurement process is composed of two steps : a reference interferogram is recorded for each chosen

polarization angle in a sample empty area, then, the sample region of interest is successively imaged following the same θ_0 angles. Reference and measurement interferograms for each given θ_0 value are associated to process final OPD images that only reveal the retardance coming from the sample. This reference set could be taken only once for the time of the experiment as long as the experimental parameters remain unchanged (magnification, sample configuration, etc...).

In the following, it will be implicit that for each interferogram image and, finally, each OPD image, a reference interferogram was taken at the corresponding polarization angle.

3.3.3. Incident polarization

A third noise source can come from a change in the reference position of the polarizer between OPD and reference acquisitions steps which is quantified using the manufacturer data $(4.4 \cdot 10^{-3} rad)$.

We said that a reference stack has to be acquired previously to the measurements. If the position of the polarizer is different between the references and the images, that can introduce a measurement bias and uncertainties. The consequences of this bad positionning have been evaluated experimentally by using interferogram association of images and references acquired with a slightly different angle corresponding to $4.4 \cdot 10^{-3} rad$ (as it was done in part 3.3.2). The mean standard deviation of the resulting OPD images was of 0.26 nm which is very close to the OPD standard deviation expected of 0.25 nm (see part 3.3.1) and do not affect the retardance measurement. Indeed, this was verified thanks to the simulation tools used and previously described in part 2.3.

3.3.4. Sample movement

The last error source is probably the most important and the most difficult to bypass. It is directly linked to the sample which can present dynamical changes during the acquisition (*i.e.* living cells and liquids movements). Such modifications that occur during the recording will be falsely interpreted as anisotropy. That is why we tried to minimize the acquisition time, keeping this error negligible. The main time-consuming step of the acquisition process is the rotation of the linear polarizer. By using only six different polarizations, we reduce the acquisition time up to 10 seconds (the exposure time generally used in the following experiments is about 50-70 ms). Typical speeds for cell motility and intracellular traffic for vesicles for instance are respectively of few μm/mn and few μm/s [35, 36]. The typical speed for cell migration is coherent with the acquisition speed of our experiment but we can see that for intracellular transports and movements, we have to be faster to limit measurement errors and image artifacts. Indeed, to avoid errors due to movement, an object (a vesicle for example) has to stay in the same pixel area during the total acquisition.

Considering two typical experimental conditions of magnification (i.e. 80x and 200x), the typical acquisition time should be inferior to 0.5 second. This can be possible using a fast camera of several hundred Hz acquisition rate and a liquid crystal reaching high switching rates instead of a rotating polarizer.

4. Results

We will suppose that it is implicit that a reference set of polarized OPD images is taken in a sample free region. We used N = 5 for the actual imaging and depending on the sample, we used either 6 or 18 different polarisations to create the set of polarized images.
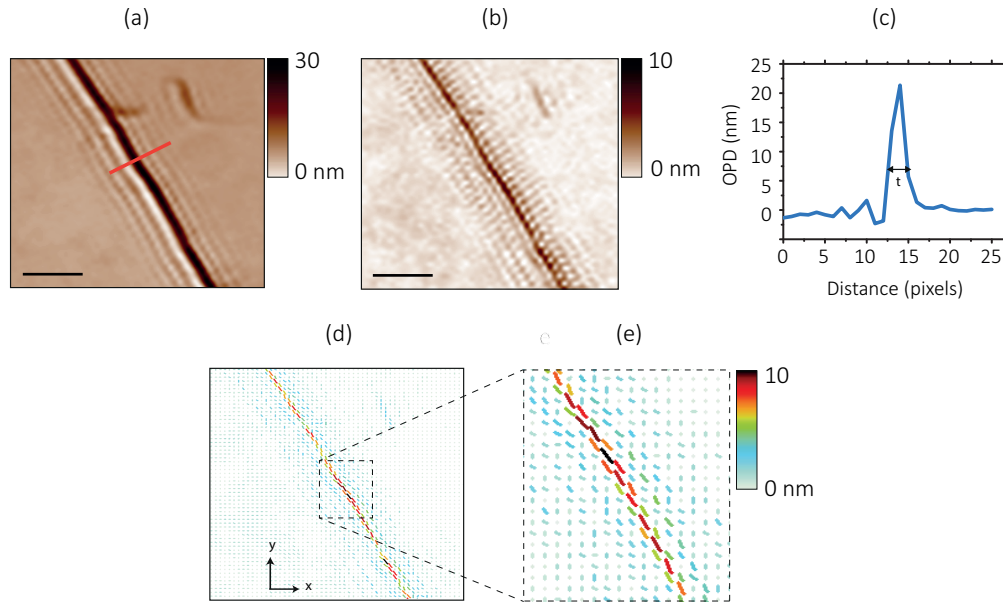
Fig. 9. Collagen fibers. (a) OPD, (b) retardance $\Delta\delta$, (c) profile along the red line on (a) and (d) & (e) orientation contrast images. Scale bar represents 5 μm. Imaging: NA=1.3, 80× magnification observation. Exposure time = 50 ms. Total acquisition time = 15 s.

4.1. Reference sample

A known reference sample was studied first. A sample of collagen fibers has been imaged first to demonstrate the reliability of our method. This sample was a Parafolmaldehyde fixed sample composed of mouse tail collagen fibers. Observation was made with a 40× with 2× supplemental magnification oil objective.

The measurement process on the field of interest takes approximately 10 seconds to acquire a set of 18 polarization dependant images. We give different representations of this sample in Fig. 9. The first image (Fig. 9(a)) represents the mean OPD value of the sample, the second one is a retardance contrast image (Fig. 9(b)); Figs. 9(d) and 9(e) images represent optical axis of the sample in the (x,y) laboratory axis system.

We can see that the linear retardance contrast image is composed by a thick line representing the collagen fiber surrounded by weaker lines which are artefacts due to diffraction. The collagen fiber is homogeneous and better localized than on the mean OPD contrast image. On the orientation image (Fig. 9(d)) the fiber optical axis is constant along the fiber and represents the direction of one of its two optical axes.

We measured on Fig. 9(b) an averaged linear retardance $\Delta\delta = 9.5 \pm 1.5$ nm along the fiber (10 retardance measurements along the fiber thanks to 10 profiles like the one of Fig. 9(c)). The retardance is constant along the fiber which can be considered as homogeneous. From several retardance images obtained with different collagen fibers of the same sample, we could extract OPD profiles.

The collagen ultrastructure is a triple helix [37] and forms tropocollagen molecules of roughly 300 nm long for 1.5 nm diameter. Each fiber is composed of tropocollagen arranged to form fibrils. At our optical resolution, the collagen structure is not accessible and the fiber appears cylindrical and homogeneous. Its diameter can be measured on OPD profile (ex. Fig. 9(c)) to determine collagen birefringence using Eq. (3).

We assumed an error of one pixel on the diameter which represents 0.30 μm and for each pixel the measurement and fitting error were calculated thanks to results of Part 3.3.3. For those retardance values, the total error was mostly dominated by the retardance measurement error. We have reported the results obtained on 4 fibers in Table 1. Finally, we were able to deduce

Table 1. Quantitative results on collagen fibers.

$\Delta\delta$ (nm)	Thickness (μm)	$\Delta n(10^{-3})$
12.8 ±0.4	3.6 ±0.3	3.6 ±0.3
10.5 ±0.4	3.2 ±0.3	3.2 ±0.3
3.6 ±0.3	1 ±0.3	3.6 ±0.1
4.5 ±0.2	1.5 ±0.3	3.0 ±0.6

a mean birefringence value of $(3.4 \pm 0.3) \cdot 10^{-3}$ which is in good agreement with the value of $3 \cdot 10^{-3}$ found in the literature [38] for collagen's birefringence.

4.2. Living samples

4.2.1. COS-7 cells

To study living samples, we choose to limit the number of excitations in order to decrease the recording duration. We know that a minimal set of three points is theoretically sufficient to fit a sinusoidal curve. However, to make a rigorous linear regression for the sinusoidal fit, we prefer to use 6 data points between 0 and π to derive the coefficients and their uncertainties. These uncertainties are used to discriminate the signal from the noise.

The technique was applied on living cells. The first sample was composed by living COS-7 cells (adherent African green monkey kidney fibroblast-like cells). Imaging and cell cultures were done in Dulbecco's Modified Eagle Medium, supplemented with 10% fetal calf serum and sodium pyruvate. The atmosphere was CO_2 and temperature controlled (5% CO_2 and 37°c) to allow long duration experiments in native cell conditions. Cells were placed in circular 35mm glass μdish (Ibidi, Planegg, Germany).

We used 6 different polarization excitations from 0° to 150° with 30° increment to create the polarization set.

The results are shown in Fig. 10. Observation was made with a 100× magnification oil objective and a 2× additional magnification. Three different representations of the same imaged field are used. The first one (Fig. 10(a)), represents the mean OPD value, the second one is a retardance contrast image (Figs. 10 (b)) and the third one, (Figs. 10 (c1, c2)) represents one optical axis of the sample in the (x,y) laboratory axis system.

We can see on the retardance image Fig. 10(b), that the cell is barely visible on this image: this was predictible since the cell components are mostly isotropic and thus non birefringent. The specific contrast enhancement created is mainly due to the plasma membrane and cytoskeleton. Those fibers seem to be stress fibers essentially composed of actin microfilaments and are responsible for the cell motility. The signal amplitude coming from fibers is weak (~ 5 nm) and focus-dependent as seen in Figs. 10(a1) and 10(b1): when the fiber is out of focus, we can observe a strong signal at the edges and low in the center. whereas when the fiber is in focus, the signal is stronger at the center. It is interesting to note that for the two fibers highlighted in crops, the optical axis orientation map gives different results and can be related to the actin monomer orientation during the polymerization.

We can see that a signal is also coming from small vesicles inside the cytoplasm. From this observation, we are unable to conclude if the signal represents a retardance signal indicating
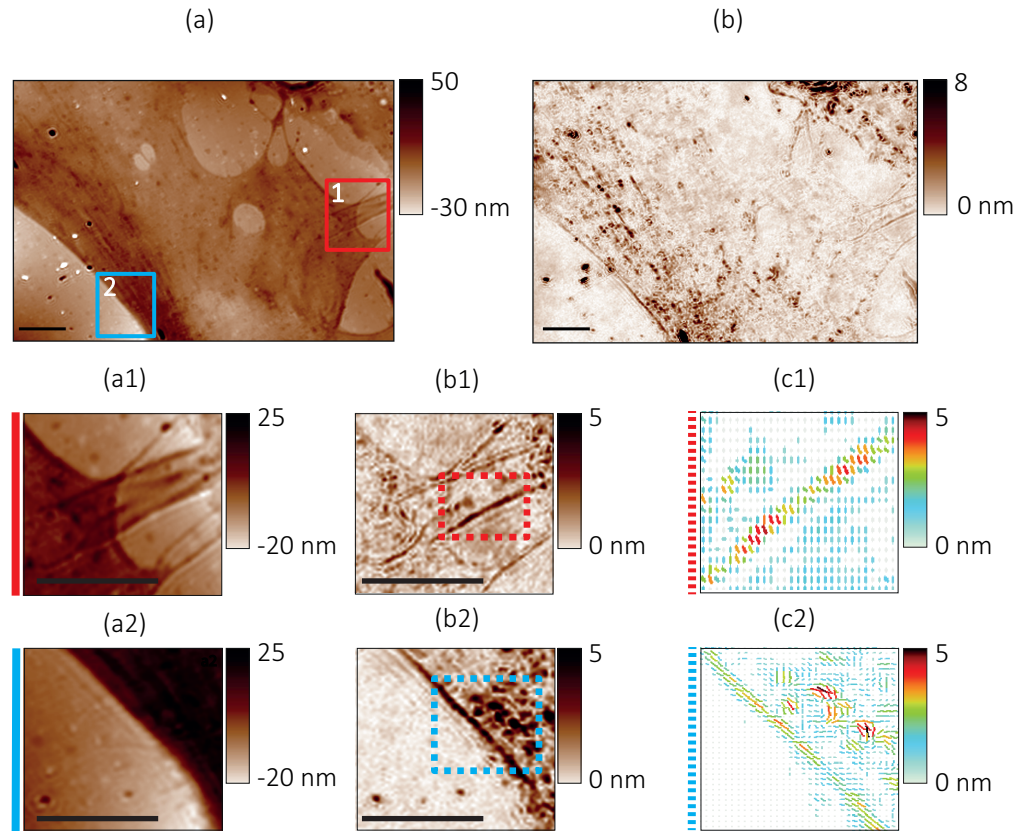
Fig. 10. (a) OPD and (b) retardance $\Delta\delta$, (a1, a2) crop and magnification following the rectangles 1 & 2 of (a), retardance (b1, b2) $\Delta\delta$, and (c1, c2) orientation of the area between dotted rectangles of images (b1) and (b2). Scale bar represents 6 μm. Imaging: NA=1.3, 200× magnification. Exposure time = 70 ms. Total acquisition time = 10 s.

that some vesicles are anisotropic or if the signal is only an artefact due to vesicles movement. A comparison with fluorescence may help to determine the nature of vesicles but this study will not be considered in this paper.

4.2.2. Multimodal OPD/fluorescence measurements on living HT1080 cells

To demonstrate the interest of the technique on a highly mobile sample, we imaged living human fibrosarcoma stable HT-1080 Lifeact cells [39], where F-actin was labelled with a GFP fusion protein. Observations were made with a 100× oil objective with a 2× additionnal magnification. The set-up for simultaneous phase and fluorescence imaging is described in details in [4].

The cells were placed in MEM + Glutamax (Invitrogen, Cergy-Pontoise, France) supplemented with 10% fetal calf serum and 0.1 mg/ml Geneticin. The atmosphere was CO_2 and temperature controlled (5% CO_2 and 37°c). The cells were placed in circular μdish support. We used 6 different polarization excitations from 0° to 150° with 30° increment. Results are shown on Fig. 11.

The first image (Fig. 11(a)) is an OPD image contrast showing that the cell is composed by many organelles such as vesicles, fibers and nucleus. The contrast is high but not specific. The
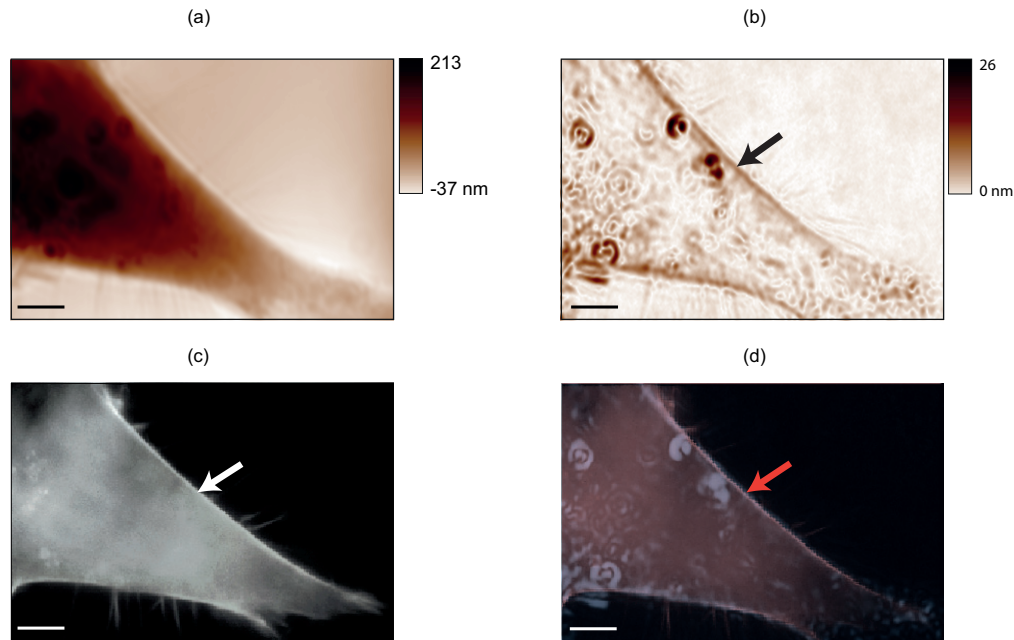
(a)

(b)

213

26

-37 nm

0 nm

(c)

(d)

Fig. 11. Living HT1080 Lifeact cell with GFP F-actin labelling. (a) OPD, (b) retardance $\Delta\delta$, (c) fluorescence and (d) composite images of (b)&(c). Scale bar represents μm. Imaging: NA=1.3, 200× magnification. Exposure time = 70 ms. Total acquisition time = 10 s.

second image is a retardance contrast image (Fig. 11(b)) showing anisotropic components in the cell. We can see that the signal is coming mostly from the plasma membrane and from some vesicles. The third image is a fluorescence contrast image (Fig. 11(c)) of F-actin labelling, showing that actin stress fibers are localised close to the plasma membrane in plasmic membrane. The last image is a composite image (images (b) and (c)).

The F-actin labelling confirms that the contrast enhanced fibers are stress fibers mainly composed by F-actin. On the composite image (Fig. 11(d)), we can see a good colocalisation of the retardance and fluorescence signals. From this observation, we can say that some fibers, assuming here stress fibers given the high fluorescence level (compared to the rest of cytoplasm) when using fluorescence labelling, are the main anisotropic component visible in living cells.

5. Conclusion

In this paper, we have described a new technique to make birefringence retardance images using a wave front sensor. This method is simple since it only needs to acquire a set of images under different excitation polarization conditions. We demonstrated its reliability to create a specific contrast enhancement of anisotropic components, and to discriminate between isotropic and anisotropic components inside biological samples, even in living ones. In particular case of collagen fibers, we can recover their intrinsic birefringence. The technique can be easily implemented on any kind of microscope and is compatible with multimodality : on the same sample, we can obtain a highly contrasted but non specific OPD image, a specific fluorescence labelling and a polarization-based set of images to identify anisotropic components.

Measurement errors have been characterized and evaluated experimentally and simulation has been used to define the retardance measurement range as 1 nm-3 μm. The relative retar-

dance measurement error determined by simulation was evaluated at less than 1% up to 2 μm.

We also applied our method to living cells showing its ability for the imaging of dynamic samples. Retardance images allow spatial localization of subcellular components, and clearly highlight stress fibers. Some progresses have to be done in the future by adding some data filtering to discriminate between anisotropic and moving components inside the sample. However, improving the rotation speed of the polarizing system will also avoid artefacts due to vesicle movements and will help to follow cells dynamic processes and stress fibers modifications. For example, liquid cristal is considered to replace the physical rotating polarizer and we hope to increase the acquisition speed by more than a decade.

A. Arbitrary polarization OPD with QWLSI

We will try in this section to simplify the expression (11):

$$\nabla OPD_{meas} = \frac{(\nabla OPD_x + \nabla OPD_y)}{2} + \frac{1}{\alpha} \arctan\left(\frac{I_x - I_y}{I_x + I_y} \cdot \tan\left((\alpha \nabla OPD_x - \alpha \nabla OPD_y)/2\right)\right) \quad (24)$$

A.1. Measured OPD in case of weak retardance gradients

We first study the case of weak retardant samples, which means that $\alpha/2(\nabla OPD^{\parallel} - \nabla OPD^{\perp})$, written in the following Δ for more readability, is small compared to 1. This hypothesis is valid in the case of cells or fibers as the typical values are about ten nanometres with low variations and thus a weak OPD gradient. Let us calculate its validity domain when $\Delta \ll 1$. We define κ as the intensity ratio $I^{\perp}/I^{\parallel}$. First, using the Taylor series of $\tan(x)$ around 0 (which is valid until $|\Delta| < \frac{\pi}{2}$)

$$S = \arctan\left(\frac{1-\kappa}{1+\kappa}\left(\Delta + \frac{\Delta^3}{3}\right)\right) + o(\Delta^3). \quad (25)$$

And then, using the Taylor series of $\arctan(x)$ around 0,

$$S \approx \frac{1-\kappa}{1+\kappa}\left(\Delta + \frac{\Delta^3}{3}\right) - \frac{1}{3}\left(\frac{1-\kappa}{1+\kappa}\right)^3 \left(\Delta - \frac{\Delta^3}{3}\right)^3 + o(\Delta^3) \quad (26)$$

$$S \approx \left(\frac{1-\kappa}{1+\kappa}\right) \Delta \left[1 + \frac{\Delta^2}{3}\left[\left(1 - \left(\frac{1-\kappa}{1+\kappa}\right)^2\right)\right]\right] + o(\Delta^3) \quad (27)$$

This relation establishes the following expression for $\nabla OPD_{measured}$ at the first order in Δ:

$$\nabla OPD_{measured} \approx \frac{(\nabla OPD^{\parallel} + \nabla OPD^{\perp})}{2} + \left(\frac{I^{\parallel} - I^{\perp}}{I^{\parallel} + I^{\perp}}\right) \cdot \Delta \quad (28)$$

And finally,

$$\nabla OPD_{measured} \approx \frac{I^{\parallel} \nabla OPD^{\parallel} + I^{\perp} \nabla OPD^{\perp}}{I^{\parallel} + I^{\perp}}. \quad (29)$$

We see that the measured OPD gradient is an average value of the gradients along the two directions $\parallel$ et $\perp$, each one is respectively weighted by the corresponding intensity component. In the case of weak intensity along one direction, the component contribution to the OPD will be weak.

Let us determine the validity domain of the previous result. We can neglect the third order term when:

$$\frac{\Delta^2}{3}\left(\frac{(1+\kappa)^2-(1-\kappa)^2}{(1+\kappa)^2}\right) << 1 \tag{30}$$

By developing the previous expression,

$$\frac{\Delta^2}{3}\left(\frac{4\kappa}{(1+\kappa)^2}\right) << 1. \tag{31}$$

Then,

$$\Delta^2 << \frac{3}{4}\frac{(1+\kappa)^2}{\kappa}. \tag{32}$$

This equation depends on κ. However, since by definition $0 \leq \kappa \leq 1$, we can estimate its boundaries. A simple variation study shows that within this range, $\frac{(1+\kappa)^2}{\kappa}$ is always higher than 4 and reaches this value for $\kappa = 1$.

In conclusion, we have $\Delta << 3$. Since $\Delta < 1$ is necessary for the Taylor expansion validity, the hypothesis that the third-order is always valid for the present application. A deeper study would be necessary for larger values but is out of the scope of this paper. The expression is expanded as:

$$1/2(\alpha(\nabla OPD^{\parallel} - \nabla OPD^{\perp})) << \sqrt{3}. \tag{33}$$

Replacing α by its expression in Eq. (33):

$$\nabla OPD_{\parallel} - \nabla OPD_{\perp} << \frac{\sqrt{3}\,p}{\pi z}. \tag{34}$$

So, the maximum difference between the OPD gradients has to be lower than a variation of 346 nm between 2 phase pixels, which is the case when considering low OPD variations of biological samples. If this variation between 2 pixels is too high, we can adjust the magnification and spread the information on more pixels to have a weaker local gradient.

A.2. *Measured OPD in case of unbalanced polarization components*

Let us try to simplify the previous expression when $\kappa << 1$, meaning that $I^{\perp} << I^{\parallel}$, and for any Δ. If $\kappa << 1$, we can write:

$$\frac{(1-\kappa)}{(1+\kappa)} = 1 - 2\kappa + o(\kappa), \tag{35}$$

$$S = \arctan\left(\frac{1-\kappa}{1+\kappa}\tan\Delta\right) = \arctan\left(\tan\Delta - 2\kappa\tan\Delta + o(\kappa)\right). \tag{36}$$

Using $\arctan(x_o + \varepsilon) = \arctan x_o + \frac{\varepsilon}{1+xo^2}$, we can write:

$$S = \Delta - 2\kappa\left(\frac{\tan\Delta}{1+\tan^2\Delta}\right). \tag{37}$$

Using, $1+\tan^2\Delta = \frac{1}{\cos^2\Delta}$, this simplifies to:

$$S = \Delta - \kappa\sin 2\Delta. \tag{38}$$

So that:

$$\nabla OPD_{meas} = \nabla OPD^{\parallel}, \tag{39}$$

$$OPD_{meas} = OPD^{\parallel}. \tag{40}$$

The validity domain of the realized approximation to consider that $\nabla OPD_{measured} = \nabla OPD^{\parallel}$ is:

$$\nabla OPD^{\parallel} \gg \frac{I^{\perp}}{I^{\parallel}} \sin(\nabla OPD^{\parallel} - \nabla OPD^{\perp}). \tag{41}$$

In the following section, we will interpret this equation in the context of the presented experiments.

B. Measure OPD after propagation through a birefringent medium

B.1. Phase along $\vec{u}^{\parallel}$

Let us consider the expression of the electric field $\vec{E}_{out}^{\parallel}$:

$$\vec{E_{out}} = ||\vec{E_{in}}||e^{\frac{ik(\delta o + \delta e)}{2}}\left(\cos\left(\frac{k\Delta\delta}{2}\right) + i\sin\left(\frac{k\Delta\delta}{2}\right)\cos 2(\theta - \theta_0)\right)\vec{u}^{\parallel}. \tag{42}$$

We choose to consider the case of small values of $\Delta\delta$. The measured OPD is:

$$OPD_{out}^{\parallel} = \frac{1}{k}arg(E_{out}^{\parallel}) = \frac{\delta o + \delta e}{2} + \frac{1}{k}\arctan\left(\tan\frac{k\Delta\delta}{2} \cdot \cos 2(\theta - \theta_0)\right). \tag{43}$$

Again we can Taylor expand this expression for small values of $\frac{k\Delta\delta}{2}$, as long as $|\frac{k\Delta\delta}{2}| < |\frac{\pi}{2}|$, which leads to:

$$OPD_{out}^{\parallel} = \frac{\delta o + \delta e}{2} + \cos 2(\theta - \theta_0) \cdot \left(\frac{k\Delta\delta}{2} + \frac{1}{3}\left(\frac{k\Delta\delta}{2}\right)^3\right) - \frac{1}{3}\cos^3 2(\theta - \theta_0)\left(\frac{k\Delta\delta}{2}\right)^3 + o\left(\frac{k\Delta\delta}{2}\right)^3, \tag{44}$$

$$OPD_{out}^{\parallel} = \frac{\delta o + \delta e}{2} + \cos 2(\theta - \theta_0) \cdot \left(\frac{k\Delta\delta}{2} + \frac{1}{12}\left(\frac{k\Delta\delta}{2}\right)^3\right) - \frac{1}{12}\cos 6(\theta - \theta_0)\left(\frac{k\Delta\delta}{2}\right)^3 + o\left(\frac{k\Delta\delta}{2}\right)^3. \tag{45}$$

Finally:

$$OPD_{out}^{\parallel} \approx \frac{\delta o + \delta e}{2} + \left(\frac{\Delta\delta}{2} + \frac{\pi^2}{\lambda^2}\frac{\Delta\delta^3}{96}\right)\cos(2(\theta - \theta_0)) - \left(\frac{\pi^2}{\lambda^2}\frac{\Delta\delta^3}{96}\right)\cos(6(\theta - \theta_0)). \tag{46}$$

In conclusion, we can consider that $OPD_{out}^{\parallel}$ is purely sinusoidal of π period if $\left(\frac{\Delta\delta^3}{96}\frac{\pi^2}{\lambda^2}\right)$ is negligible in front of $\frac{\Delta\delta}{2}$ and until: $\Delta\delta \ll \frac{4\sqrt{3}\lambda}{\pi}$, with $\frac{4\sqrt{3}}{\pi} \approx 2,2$.

As a conclusion, for retardance values such as $\Delta\delta < 2,2\lambda$, OPD varies as a sinusoidal function of the incident polarization angle:

$$OPD_{measured}(\theta) = \frac{(\delta o + \delta e)}{2} + \left(\frac{\Delta\delta}{2}\right)\cos 2(\theta - \theta_0). \tag{47}$$

We showed previously (Eq. (41)) that we could neglect the field component along $\vec{u}^{\perp}$ if

$$\nabla OPD^{\parallel} >> \frac{I^{\perp}}{I^{\parallel}} \sin(\nabla OPD^{\parallel} - \nabla OPD^{\perp}) \tag{48}$$

Let us study the validy domain of this hypothesis in the frame of our birefringence technique. We will evaluate the previous inequation with the corresponding values :

$$\begin{cases} OPD^{\parallel} = \dfrac{(\delta o + \delta e)}{2} + (\dfrac{\Delta \delta}{2}) \cos 2(\theta - \theta_0), \\ OPD^{\perp} = \dfrac{(\delta o + \delta e)}{2} + \dfrac{\pi}{2}, \\ OPD^{\parallel} - OPD^{\perp} = (\dfrac{\Delta \delta}{2}) \cos 2(\theta - \theta_0) - \dfrac{\pi}{2}, \end{cases}$$

and

$$\begin{cases} I_x = \cos^2(\dfrac{k\Delta \delta}{2}) + \sin^2(\dfrac{k\Delta \delta}{2}) \sin^2 2(\theta - \theta_0), \\ I_y = \sin^2(\dfrac{k\Delta \delta}{2}) \sin^2 2(\theta - \theta_0). \end{cases}$$

In the case of weak $\Delta\delta$,

$$\begin{cases} I^{\parallel} \approx 1 - I^{\perp} \approx 1, \\ I^{\perp} \approx \dfrac{k^2 \Delta \delta^2}{4} \sin^2 2(\theta - \theta_0), \end{cases}$$

and we can write:

$$\frac{k^2 \Delta \delta^2}{4} \frac{\nabla(\Delta \delta)}{2} << \nabla OPD^{\parallel}. \tag{49}$$

Using $\overline{\delta} = \frac{(\delta o + \delta e)}{2} \approx OPD^{\parallel}$ as the OPD averaged value, L_B and L_{OPD} respectively the birefringence and OPD typical lengths which represent the typical size of birefringent structures and phase objects, we write:

$$\frac{k^2 \Delta \delta^2}{8} \frac{\Delta \delta}{L_B} << \frac{\overline{\delta}}{L_{OPD}}. \tag{50}$$

We now assume that $L_{OPD} \approx L_B$, which means that the phase and birefringent structures have the same typical size. This is true in practice since for instance fibers are equally visible in phase and birefringence retardance images. We finally obtain the following expression:

$$\left(\frac{\Delta \delta}{\overline{\delta}}\right)^3 << \frac{8}{k^2 \, \overline{\delta}^2}. \tag{51}$$

$$\left(\frac{\Delta \delta}{\overline{\delta}}\right) << \sqrt[3]{\frac{2\lambda^2}{\pi^2 \overline{\delta}^2}} \tag{52}$$

However,

$$\frac{\Delta \delta}{\overline{\delta}} = \frac{\Delta n \times e}{\overline{n} \times e} = \frac{\Delta n}{n} \tag{53}$$

Finally,

$$\frac{\Delta n}{\overline{n}} << \sqrt[3]{\frac{2}{\pi^2}} \; (\frac{\lambda}{\overline{\delta}})^{2/3}. \tag{54}$$

We can make a numerical application with $\overline{\delta}$=10 μm, λ=0,7 μm. We find

$$\frac{\Delta n}{\overline{n}} << 0.1 \tag{55}$$

This value is in accordance with refractive expected values of about 10^{-2}-10^{-3} and 1,3-1,5 for respectively Δn and n in biological media.

In conclusion, this inequality is always true in the case of biological samples. This means that for biological samples the perpendicular components is negligible and the measured OPD corresponds to the OPD induced on the parallel component.